



## Mechanical properties and wear resistance of medium entropy Fe<sub>40</sub>Mn<sub>40</sub>Cr<sub>10</sub>Co<sub>10</sub>/TiC composites

Jian-ying WANG<sup>1</sup>, Jing-hua FANG<sup>1</sup>, Hai-lin YANG<sup>1</sup>,  
Zhi-lin LIU<sup>2</sup>, Rui-di LI<sup>1</sup>, Shou-xun JI<sup>3</sup>, Yun WANG<sup>3</sup>, Jian-ming RUAN<sup>1</sup>

1. State Key Laboratory of Powder Metallurgy, Central South University, Changsha 410083, China;
2. School of Mechanical and Electrical Engineering, Central South University, Changsha 410083, China;
3. Institute of Materials and Manufacturing, Brunel University London, Uxbridge, Middlesex UB8 3PH, U. K.

Received 6 September 2018; accepted 8 January 2019

**Abstract:** The Fe<sub>40</sub>Mn<sub>40</sub>Cr<sub>10</sub>Co<sub>10</sub>/TiC (volume fraction of TiC, 10%) composites were synthesized in combination of ball milling and spark plasma sintering (SPS) in the present work. Mechanical properties and wear resistance of the Fe<sub>40</sub>Mn<sub>40</sub>Cr<sub>10</sub>Co<sub>10</sub>/TiC composites were individually investigated. It was found that TiC particles homogeneously distributed in the Fe<sub>40</sub>Mn<sub>40</sub>Cr<sub>10</sub>Co<sub>10</sub>/TiC composite after being sintered at 1373 K for 15 min. Meanwhile, grain refinement was observed in the as-sintered composite. Compared with the pure Fe<sub>40</sub>Mn<sub>40</sub>Cr<sub>10</sub>Co<sub>10</sub> medium entropy alloy (MEA) matrix grain, addition of 10% TiC particles resulted in an increase in the compressive strength from 1.571 to 2.174 GPa, and the hardness from HV 320 to HV 872. Wear resistance results demonstrated that the friction coefficient, wear depth and width of the composite decreased in comparison with the Fe<sub>40</sub>Mn<sub>40</sub>Cr<sub>10</sub>Co<sub>10</sub> MEA matrix. Excellent mechanical properties and wear resistance could offer the Fe<sub>40</sub>Mn<sub>40</sub>Cr<sub>10</sub>Co<sub>10</sub>/TiC composite a very promising candidate for engineering applications.

**Key words:** TiC; Fe<sub>40</sub>Mn<sub>40</sub>Cr<sub>10</sub>Co<sub>10</sub>/TiC composites; mechanical properties; wear resistance; spark plasma sintering

### 1 Introduction

High entropy alloys (HEAs)/medium entropy alloys (MEAs) have been accepted great interest in research as a new class of metallic alloys. The unique feature of the MEAs/HEAs is the simple solid solution (FCC/BCC/HCP) phase comprising of multiple equiatomic or near-equiatomic elements with high configurational entropy. This is significantly different from the conventional alloys consisting of principal elements and minor elements and often crystallized in the formation of solid solution and intermetallic phases [1,2]. Although a number of advantages of HEA/MEAs have been well recognized, the drawbacks of HEA/MEAs including relatively low strength and poor wear resistance, have limited their applications as strong candidates of structural materials. Therefore, the attempts to improve the strength are becoming important in industrial applications.

It has been confirmed that metal matrix composites (MMCs) can offer outstanding mechanical properties and superior wear resistance [3–5]. The alloys reinforced by particulates, such as SiC [6], TiB<sub>2</sub> [7], WS<sub>2</sub> [8], B<sub>4</sub>C [9] and Al<sub>2</sub>O<sub>3</sub> [10], have been used in various applications. The introduction of particulates into a single phase matrix of HEA/MEAs can be an effective approach to improve mechanical properties, in particular the wear resistance. Recently, the effect of reinforcement particles on the microstructure and wear resistance of the HEA/MEAs has been the topics of a number of investigations. LIU et al [11] introduced brittle  $\sigma$  and  $\mu$  phases into a FCC-structured CoCrFeNi MEA through addition of Mo particles. The particle-strengthened alloy exhibits a tensile strength as high as 1.2 GPa and a tensile elongation of ~19%. ROGAL et al [12,13] pointed out that 5% Al<sub>2</sub>O<sub>3</sub> (mass fraction) and 5% SiC (mass fraction) particles were uniformly distributed in CoCrFeMnNi HEA, which delivered compressive yield stress and compressive strain as high as 1480 MPa

and 1600 MPa, and 31% and 6.5%, respectively. COLOMBINI et al [14] studied the FeCoNiCrAl high entropy alloy reinforced by reactive silicon carbide (SiC) particles through a powder metallurgy synthetic route. The reactive sintering produced a single isomorphous BCC structure and formed stable carbides and silicide particles, which increased the hardness of the alloy. CoCrFeNi self-lubricating composite reinforced by graphite and MoS<sub>2</sub> powder has good mechanical and tribological properties [15].

Fe<sub>40</sub>Mn<sub>40</sub>Cr<sub>10</sub>Co<sub>10</sub> is a newly developed MEA with the features of excellent elongation (57.7%) but low yield strength (213 MPa) [16]. It is interesting to study the effect of TiC particles on the reinforcement of Fe<sub>40</sub>Mn<sub>40</sub>Cr<sub>10</sub>Co<sub>10</sub> MEA, in particular the wear resistance. In the present work, Fe<sub>40</sub>Mn<sub>40</sub>Cr<sub>10</sub>Co<sub>10</sub>/TiC composites were processed by spark plasma sintering (SPS) to obtain fully dense materials at relatively low temperature and a short time. Mechanical properties and wear resistance of the FCC-type Fe<sub>40</sub>Mn<sub>40</sub>Cr<sub>10</sub>Co<sub>10</sub>/TiC composite were assessed in association with the microstructure. The strength and hardness of the composites were compared with those of Fe<sub>40</sub>Mn<sub>40</sub>Cr<sub>10</sub>Co<sub>10</sub> MEA. Discussion focused on the effect of TiC on the strengthening mechanism and the improvement in tribological behavior.

## 2 Experimental

### 2.1 Materials and composites manufacturing

The water-atomized Fe<sub>40</sub>Mn<sub>40</sub>Cr<sub>10</sub>Co<sub>10</sub> MEA powder (with the average particle size of 5–15 μm) and TiC (99.5 wt.%) particles were used as starting materials. The size of TiC particles is mainly 1–4 μm. Fe<sub>40</sub>Mn<sub>40</sub>Cr<sub>10</sub>Co<sub>10</sub> MEA and Fe<sub>40</sub>Mn<sub>40</sub>Cr<sub>10</sub>Co<sub>10</sub>/10% TiC composite were fabricated by planetary ball milling and SPS. Alcohol was employed as the process control agent (PCA) to avoid welding and oxidation of the powder. The powder was mixed by ball milling for 6 h, followed by consolidating into discs of 40 mm in diameter using SPS at 1373 K for 15 min with a uniaxial pressure of 40 MPa.

### 2.2 Microstructure characterization

X-ray diffractometer (XRD, Rigaku X-2000) and scanning electron microscope (SEM, FEI nano 230 field emission) equipped with an energy dispersive X-ray (EDAX) spectrometer were used to characterize the microstructure and phase composition. Electron backscattered diffraction (EBSD) was conducted to access the grain structure using a Hitachi S-3400N SEM instrument equipped with a HKL-EABS system. The microstructure and selected area electron diffraction (SADP) were observed using a Tecnai G2 F20 transmission electron microscope (TEM). To prepare

thin foil specimens for TEM examination, slices cut from the as-SPSed alloy samples were mechanically ground and cut into discs with 3 mm in diameter. These discs were then ground to a thickness less than 60 μm and finally ion-beam thinned using a Gatan precision ion polishing system (PIPS) at a voltage of 5 kV and an incident angle of 3°–7°.

### 2.3 Mechanical properties test

An Instron® 3369 universal testing machine was used for testing the compressive mechanical properties of Fe<sub>40</sub>Mn<sub>40</sub>Cr<sub>10</sub>Co<sub>10</sub> MEA and Fe<sub>40</sub>Mn<sub>40</sub>Cr<sub>10</sub>Co<sub>10</sub>/10%TiC composite, with a cross-head speed of 1 mm/min. The size of the cylindrical sample was  $d5 \text{ mm} \times 7 \text{ mm}$ . The hardness tests were carried out using an HVS-5 hardness tester with the load being 49 N for 10 s. All the reported data were the average of at least 5 specimens.

### 2.4 Wear resistance test

Wear tests were carried out using an HRS-2M roller friction wear tester at room temperature with a rotation speed of 600 r/min, a test load of 10 N, a duration time of 5 min and a total sliding distance of 60 m. The counter body of roller was a Si<sub>3</sub>N<sub>4</sub> ball with a diameter of 5 mm.

## 3 Results

### 3.1 Microstructure characterization

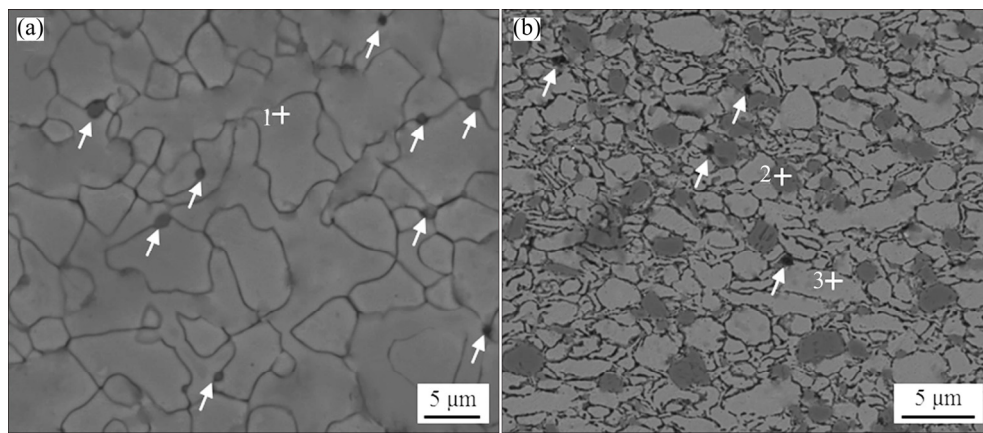
SEM-BSE images in Fig. 1 show the microstructure of Fe<sub>40</sub>Mn<sub>40</sub>Cr<sub>10</sub>Co<sub>10</sub> MEA without and with 10% TiC particles. The microstructure of Fe<sub>40</sub>Mn<sub>40</sub>Cr<sub>10</sub>Co<sub>10</sub> MEA exhibited a homogenous single phase. Pores were observed in the as-SPSed alloy, as marked by the arrows in Fig. 1(a). With the addition of TiC particles, obvious changes in the microstructure were observed in comparison with Fe<sub>40</sub>Mn<sub>40</sub>Cr<sub>10</sub>Co<sub>10</sub> MEA. The Fe<sub>40</sub>Mn<sub>40</sub>Cr<sub>10</sub>Co<sub>10</sub> matrix powder was present in a softening state at sintering temperature during SPS process. Under an external pressure during SPS, TiC particles filled the pores/gaps between their neighboring matrix powder particles to form more compact mixed powder particles. Thus, the grains were refined considerably and much less pores were found in the composite (Fig. 1(b)).

Table 1 gives the chemical compositions of various phases measured by SEM-EDS analysis. The analyzed results from the matrix at Point 1 in Fig. 1(a) are consistent with the initial proportion of alloy powder ( $n(\text{Fe}):n(\text{Mn}):n(\text{Cr}):n(\text{Co})=4:4:1:1$ ). Analysis from the dark grey phase at Point 2 in Fig. 1(b) shows that the phase consists mainly of carbon and titanium. Similarly, the composition at Point 3 in Fig. 1(b) is roughly satisfied with the alloy composition of  $n(\text{Fe}):n(\text{Mn}):$

$n(\text{Cr}):n(\text{Co})=4:4:1:1$ . It was also seen that the two phases in Fig. 1(b) contained other elements. For example, there were a small quantity of Fe, Mn, Cr and Co in the TiC phase. There were also Ti and C in the matrix phase. This could be attributed to two reasons: one is the measure error as the phase is too fine for SEM beam; the other is that atomic diffusion is resulted from the added particles and the matrix alloy during the sintering process at high temperature, indicating that the interaction between the added particles and the matrix alloy occurred. Elemental mapping on the selected area of the composite was further carried out by SEM-EDS. As shown in Fig. 2, Fe, Cr and Co elements distributed uniformly in the matrix

grains; however, Mn and O mainly segregated to the matrix grain boundaries. Due to the high chemical affinity between Mn and O atoms, some MnO may be expected to develop at the matrix grain boundaries. The dark gray phase was composed of Ti and C, confirming that the dark grey phase in Fig. 1(b) was TiC.

The XRD patterns of  $\text{Fe}_{40}\text{Mn}_{40}\text{Cr}_{10}\text{Co}_{10}$  and  $\text{Fe}_{40}\text{Mn}_{40}\text{Cr}_{10}\text{Co}_{10}/10\%$  TiC composite are shown in Fig. 3.  $\text{Fe}_{40}\text{Mn}_{40}\text{Cr}_{10}\text{Co}_{10}$  MEA only showed the peaks of a FCC phase, implying that no other phases were formed except for the matrix phase. This was in good agreement with medium entropy alloy and also agreed with the previous study [16]. On the other hand,  $\text{Fe}_{40}\text{Mn}_{40}\text{Cr}_{10}\text{Co}_{10}/$



**Fig. 1** Backscattered SEM micrographs showing microstructure of  $\text{Fe}_{40}\text{Mn}_{40}\text{Cr}_{10}\text{Co}_{10}$  MEA (a) and  $\text{Fe}_{40}\text{Mn}_{40}\text{Cr}_{10}\text{Co}_{10}/10\%$  TiC composite (b) (Arrows mark porosities. “+” marks are locations for composition analysis)

**Table 1** EDS results of  $\text{Fe}_{40}\text{Mn}_{40}\text{Cr}_{10}\text{Co}_{10}/10\%$ TiC composite corresponding to Fig. 1 (at.%)

Point in Fig. 1	Fe	Mn	Cr	Co	Ti	C
1	40.33	38.26	11.12	10.29	–	–
2	01.94	01.82	01.09	00.55	49.09	45.51
3	39.16	32.75	09.37	05.94	05.02	07.76

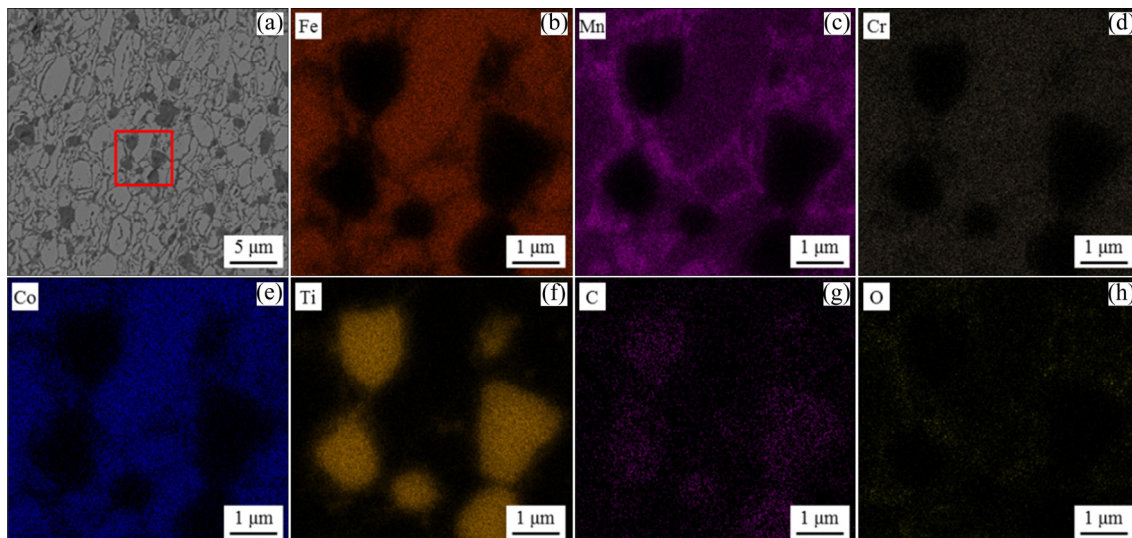


**Fig. 2** SEM-EDS mapping images showing element distribution of  $\text{Fe}_{40}\text{Mn}_{40}\text{Cr}_{10}\text{Co}_{10}/10\%$  TiC composite: (a) SEM image; (b-h) EDS mapping images

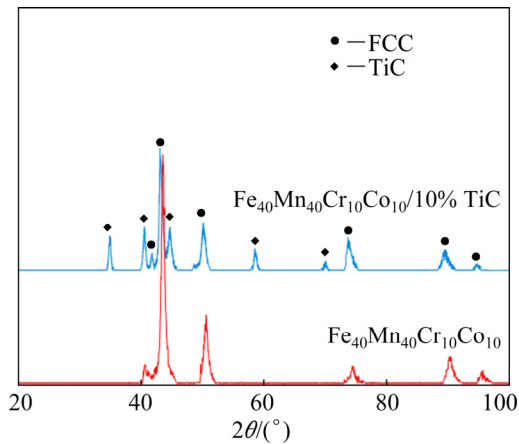


**Fig. 3** XRD patterns of  $\text{Fe}_{40}\text{Mn}_{40}\text{Cr}_{10}\text{Co}_{10}$  MEA and  $\text{Fe}_{40}\text{Mn}_{40}\text{Cr}_{10}\text{Co}_{10}/10\%$  TiC composite

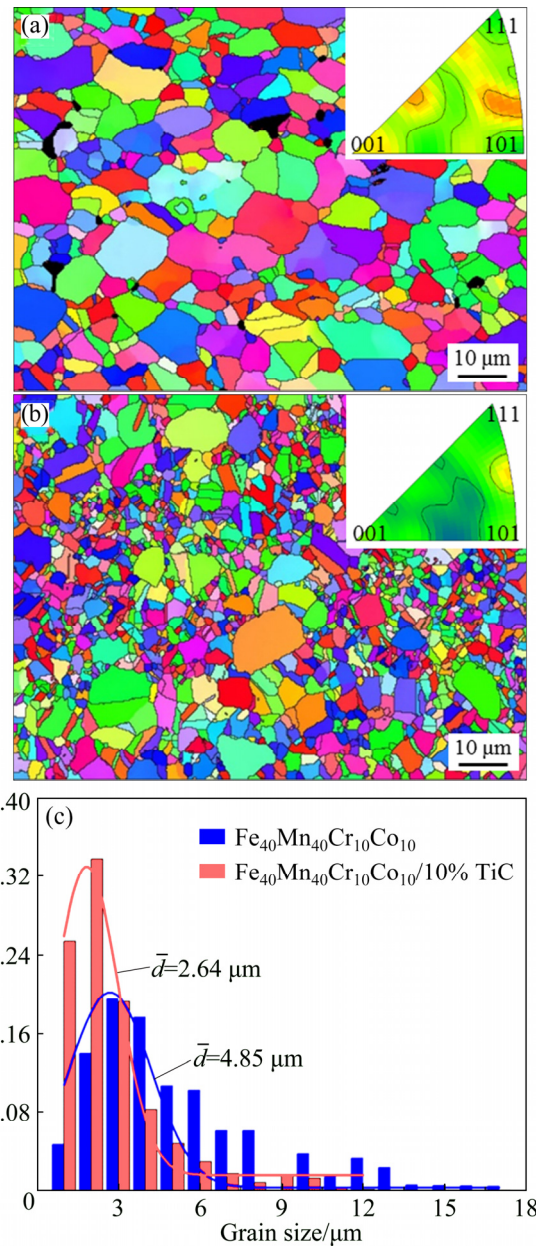
10% TiC composite consisted of FCC phase and TiC phase with no other phases.

EBSDB results in Fig. 4 show the grain structure of  $\text{Fe}_{40}\text{Mn}_{40}\text{Cr}_{10}\text{Co}_{10}/10\%$  TiC composite in comparison with  $\text{Fe}_{40}\text{Mn}_{40}\text{Cr}_{10}\text{Co}_{10}$  MEA. The addition of the TiC particles resulted in an obvious grain refinement and much less pores for the composite. The average grain sizes of the FCC phase were 4.85  $\mu\text{m}$  for  $\text{Fe}_{40}\text{Mn}_{40}\text{Cr}_{10}\text{Co}_{10}$  MEA and 2.64  $\mu\text{m}$  for the composite. The inverse pole figures (IPFs) of the FCC phase shown as inserts in Fig. 4 confirmed that the FCC grains have no obvious preferred orientation in  $\text{Fe}_{40}\text{Mn}_{40}\text{Cr}_{10}\text{Co}_{10}$  with and without TiC addition.

TEM bright field image in Fig. 5(a) shows the microstructure of  $\text{Fe}_{40}\text{Mn}_{40}\text{Cr}_{10}\text{Co}_{10}$  MEA, and the SADP (insert in Fig. 5(a)), taken from area  $L_1$ , verified the FCC structure. TEM bright field image taken from the composite is shown in Fig. 5(b), where two phases can be seen in the microstructure. The SADP from area  $L_2$  showed that the matrix was also FCC structure. The dark particles marked as  $L_3$  were identified as TiC, with the SADPs shown in the insert. High resolution TEM (HRTEM) images in Figs. 5(c) and (d) show the interface between TiC particles and the FCC matrix. It is seen that the interface is sharp and clean (without secondary phase). Fast Fourier transformation (FFT) patterns from the lattice image confirm the orientation relationship of the FCC solid solution and TiC particle. The FCC phase is along the [011] zone axis (see  $L_4$ ) and TiC is along its  $[\bar{1}22]$  zone axis (see  $L_5$ ).

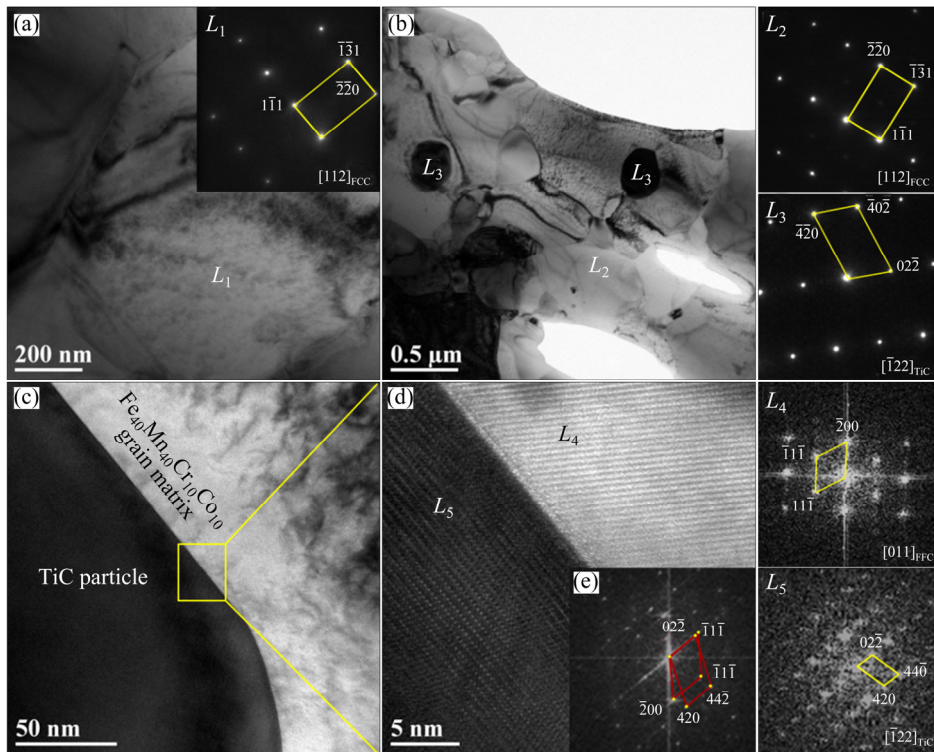
### 3.2 Mechanical properties

Figure 6 shows the compressive stress–strain curves of  $\text{Fe}_{40}\text{Mn}_{10}\text{Cr}_{10}\text{Co}_{10}$  with addition of TiC in comparison with some other HEA/MEAs.  $\text{Fe}_{40}\text{Mn}_{40}\text{Cr}_{10}\text{Co}_{10}$  MEA had a compressive strength of 1.571 GPa with corresponding compressive strain of 28.5%. The addition



**Fig. 4** EBSD mapping-based microstructures showing variation of grain sizes of  $\text{Fe}_{40}\text{Mn}_{40}\text{Cr}_{10}\text{Co}_{10}$  MEA (a),  $\text{Fe}_{40}\text{Mn}_{40}\text{Cr}_{10}\text{Co}_{10}/10\%$  TiC composite (b) and distribution of average grain size (c) (Inserts in (a) and (b) are inverse pole figures (IPFs) of FCC phase in alloy)

of 10% TiC led to an obvious increase in compressive strength to 2.174 GPa and a slight increase in compressive strain to 32.2% for the composite. Considering the fact that compressive strain normally decreases with the addition of the ceramic particles, a slight increase in compressive strain could be ascribed to two factors. One is the effect of grain refinement, the other is the reduction of pores. As shown in Table 2, the hardness is also significantly increased from HV 320 to HV 872. The difference in fracture morphology is shown in Figs. 6(c) and (d).  $\text{Fe}_{40}\text{Mn}_{40}\text{Cr}_{10}\text{Co}_{10}$  MEA showed a



**Fig. 5** TEM bright field micrographs of  $\text{Fe}_{40}\text{Mn}_{40}\text{Cr}_{10}\text{Co}_{10}$  MEA with SADP revealing single FCC solid solution (a),  $\text{Fe}_{40}\text{Mn}_{40}\text{Cr}_{10}\text{Co}_{10}/10\%$  TiC composite with corresponding SADP patterns (b) and image showing interfacial relationship between matrix phase and TiC (c), TEM high resolution image of rectangular area (d) in (c) and indexed schematic of corresponding interface relationship (e)

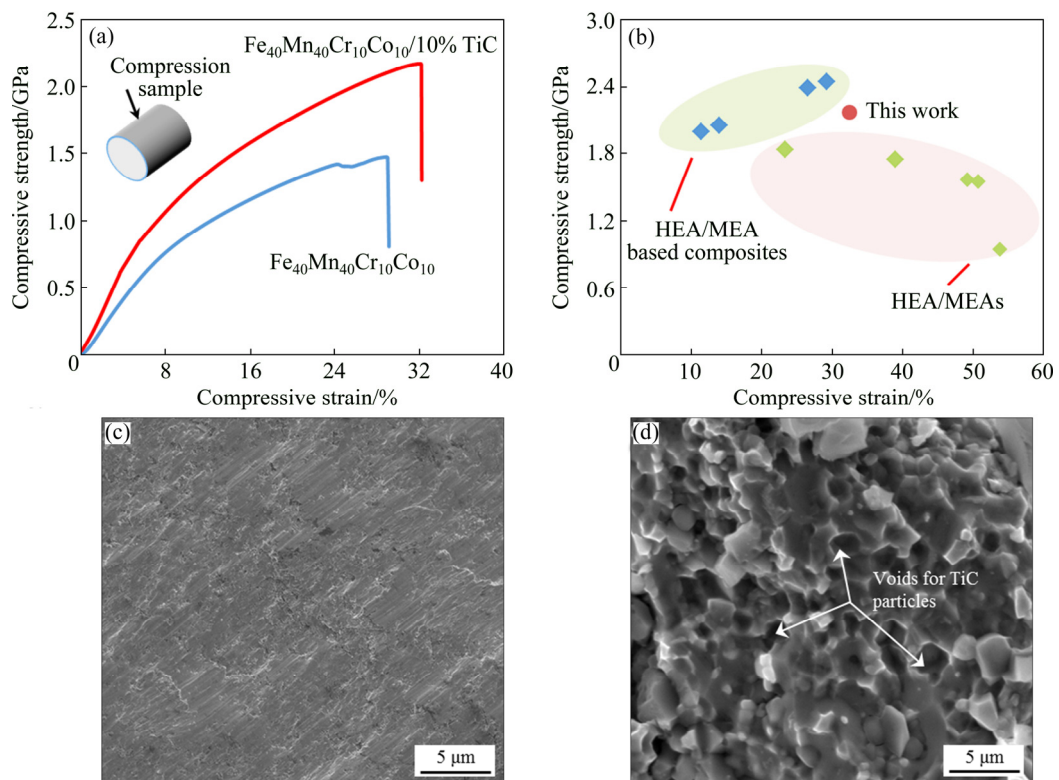


**Fig. 6** Compressive stress–strain curves of  $\text{Fe}_{40}\text{Mn}_{40}\text{Cr}_{10}\text{Co}_{10}$  MEA and  $\text{Fe}_{40}\text{Mn}_{40}\text{Cr}_{10}\text{Co}_{10}/10\%$  TiC composite (a), comparison of compressive strength vs compressive strain of typical HEA/MEAs [17–19] and HEA/MEA based composites [12–13, 20–21] (b), fracture surfaces of as-sintered  $\text{Fe}_{40}\text{Mn}_{40}\text{Cr}_{10}\text{Co}_{10}$  (c) and  $\text{Fe}_{40}\text{Mn}_{40}\text{Cr}_{10}\text{Co}_{10}/10\%$  TiC (d) (Voids of post-deformed samples are highlighted by white arrows in (d))

single slip fracture surface, and the fracture consisted of a large number of slip bands. While the fracture surface of the composite was of a typical ductile-brittle mode. Moreover, there were many voids left on the surface of the composite after TiC particles were pulled out.

### 3.3 Wear resistance

Figure 7 shows the 3D optical wear tracks and the corresponding 2D cross-section depth profiles of  $\text{Fe}_{40}\text{Mn}_{40}\text{Cr}_{10}\text{Co}_{10}$  MEA and  $\text{Fe}_{40}\text{Mn}_{10}\text{Cr}_{10}\text{Co}_{10}/10\%$  TiC composite under a load of 10 N. As expected, the wear track of  $\text{Fe}_{40}\text{Mn}_{40}\text{Cr}_{10}\text{Co}_{10}$  MEA was deeper than that of the composite. The depth of  $\text{Fe}_{40}\text{Mn}_{40}\text{Cr}_{10}\text{Co}_{10}$  MEA was 1.9 about times that of  $\text{Fe}_{40}\text{Mn}_{10}\text{Cr}_{10}\text{Co}_{10}/10\%$  TiC composite. The friction coefficients were 0.6 and 0.26 for  $\text{Fe}_{40}\text{Mn}_{40}\text{Cr}_{10}\text{Co}_{10}$  MEA and the composite, respectively (see Table 3). The reduced depth and friction coefficient confirmed that the wear resistance of the composite was improved.

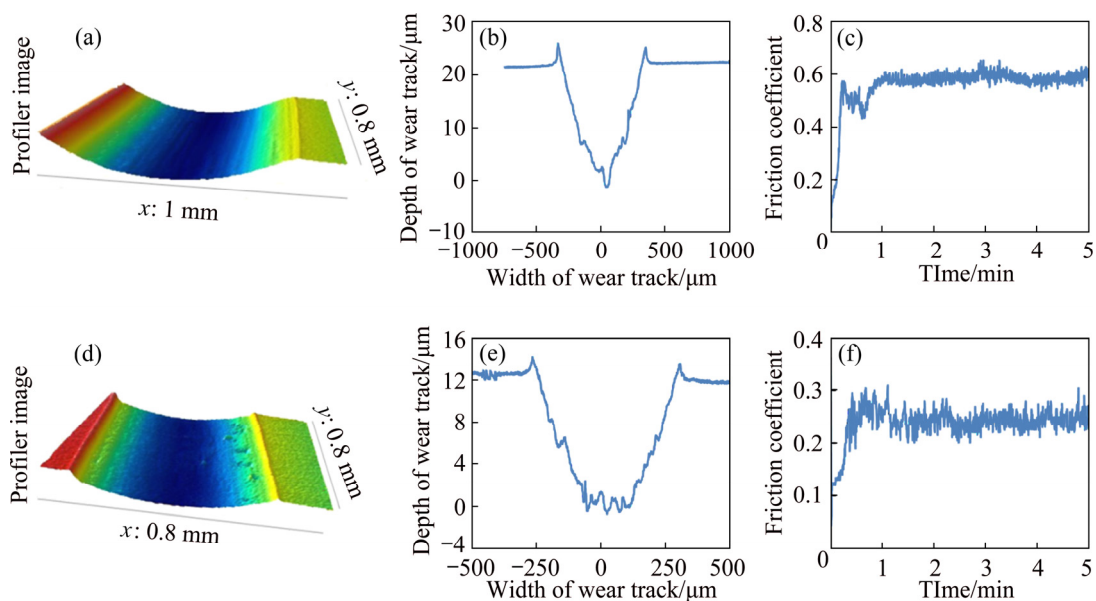
SEM images in Fig. 8 show the morphologies of the wear tracks. For  $\text{Fe}_{40}\text{Mn}_{40}\text{Cr}_{10}\text{Co}_{10}$  MEA, numerous wear particles and micro-ploughing were found inside the wear track (Fig. 8(a)). However, there were no visible micro-ploughs and wear particles on the worn surface of the composite (Fig. 8(d)). SEM images of the wear track

at higher magnification in Figs. 8(b) and (e) showed that wear particles were clearly visible inside the wear track of  $\text{Fe}_{40}\text{Mn}_{40}\text{Cr}_{10}\text{Co}_{10}$  MEA. These particles were identified as metallic oxides based on the SEM–EDS results shown in Fig. 8(c). The observation of the worn surface indicates that the wear modes of  $\text{Fe}_{40}\text{Mn}_{40}\text{Cr}_{10}\text{Co}_{10}$  MEA included abrasive wear and oxidation wear, while the worn surface of the composite (Fig. 8(e)) was rough, which may be caused by the debonding of TiC and matrix. And the shedding TiC particles acted as abrasive particles and the primary wear mode of the composite was abrasion wear.

The XPS analysis results of  $\text{Fe}_{40}\text{Mn}_{40}\text{Cr}_{10}\text{Co}_{10}$  MEA and  $\text{Fe}_{40}\text{Mn}_{40}\text{Cr}_{10}\text{Co}_{10}/10\%$  TiC composite are shown in Figs. 9 and 10, respectively. From Fig. 9, the metallic oxides (mainly  $\text{Fe}_2\text{O}_3$ ,  $\text{Cr}_2\text{O}_3$  and  $\text{Mn}_2\text{O}_3$ ) were formed on the worn surface, which was in good agreement with the SEM–EDS results in Fig. 8(c). Similarly, the metallic oxides were also found on the worn surface of  $\text{Fe}_{40}\text{Mn}_{40}\text{Cr}_{10}\text{Co}_{10}/10\%$  TiC composites (Fig. 10), although no wear particles were visible in Fig. 8(e). The results of XPS showed that both  $\text{Fe}_{40}\text{Mn}_{40}\text{Cr}_{10}\text{Co}_{10}$  and  $\text{Fe}_{40}\text{Mn}_{40}\text{Cr}_{10}\text{Co}_{10}/10\%$  TiC composite were obviously oxidized during wear test. Therefore, oxidation wear is the major wear mechanism for  $\text{Fe}_{40}\text{Mn}_{40}\text{Cr}_{10}\text{Co}_{10}/10\%$  TiC composite.

**Table 2** Mechanical properties of  $\text{Fe}_{40}\text{Mn}_{10}\text{Cr}_{10}\text{Co}_{10}$  MEA and  $\text{Fe}_{40}\text{Mn}_{10}\text{Cr}_{10}\text{Co}_{10}/10\%$  TiC composite

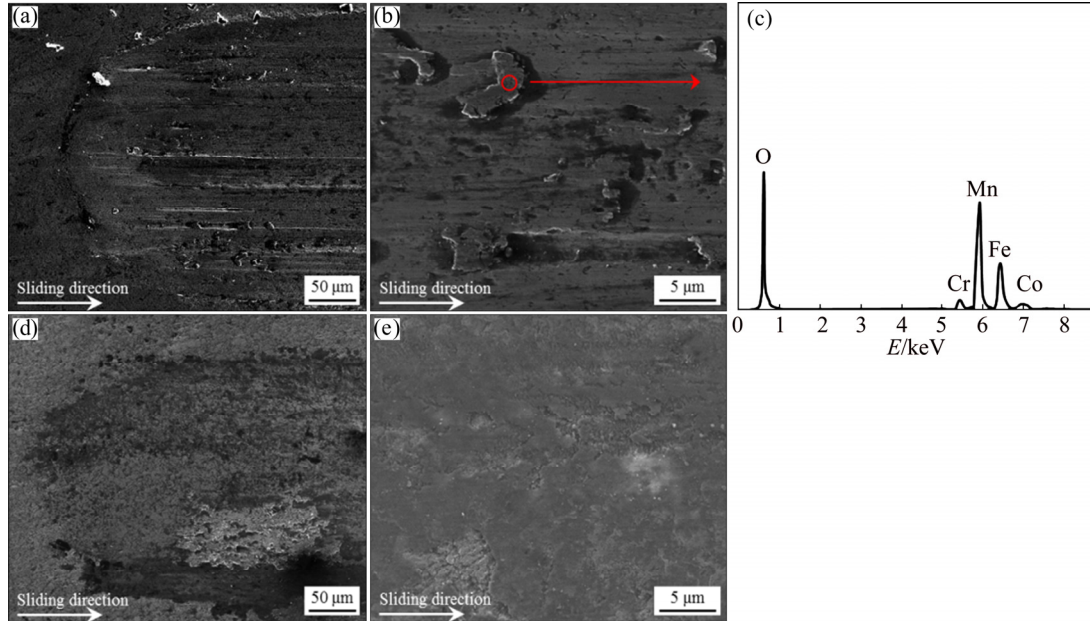
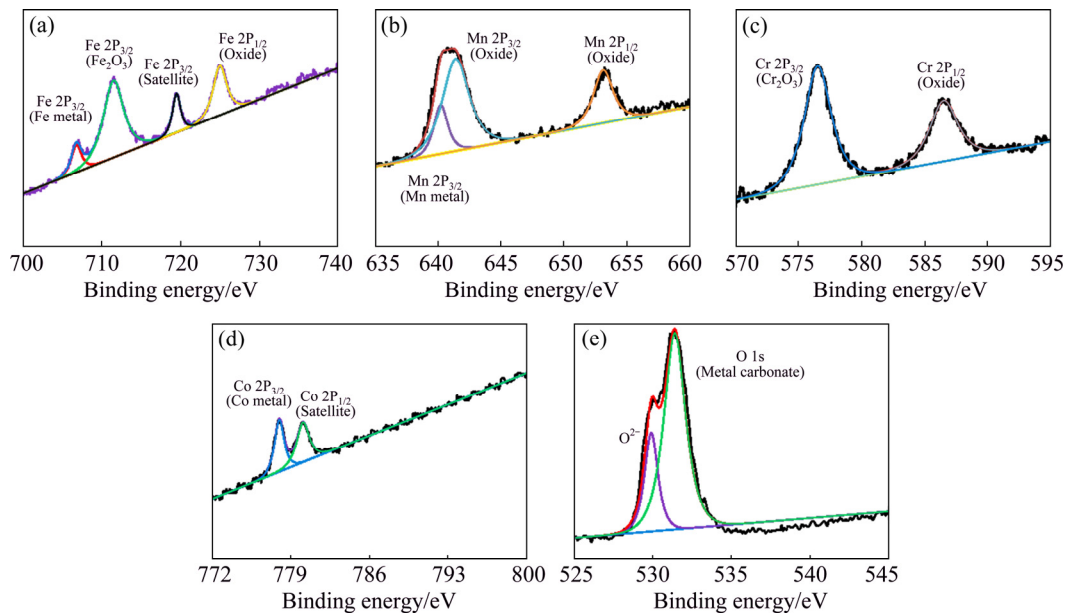
Alloy	Yield strength/GPa	Compressive strength/GPa	Compressive strain/%	Hardness (HV)
$\text{Fe}_{40}\text{Mn}_{10}\text{Cr}_{10}\text{Co}_{10}$ MEA	0.48	1.571	28.5	320
$\text{Fe}_{40}\text{Mn}_{10}\text{Cr}_{10}\text{Co}_{10}$ MEA/10% TiC	0.73	2.174	32.2	872



**Fig. 7** 3D optical wear tracks of  $\text{Fe}_{40}\text{Mn}_{40}\text{Cr}_{10}\text{Co}_{10}$  MEA (a) and  $\text{Fe}_{40}\text{Mn}_{40}\text{Cr}_{10}\text{Co}_{10}/10\%$  TiC composite (d) under 10 N load, cross-section depth profiles of  $\text{Fe}_{40}\text{Mn}_{40}\text{Cr}_{10}\text{Co}_{10}$  MEA (b) and  $\text{Fe}_{40}\text{Mn}_{40}\text{Cr}_{10}\text{Co}_{10}/10\%$  TiC composite (e), and fraction coefficients of  $\text{Fe}_{40}\text{Mn}_{40}\text{Cr}_{10}\text{Co}_{10}$  MEA (c) and  $\text{Fe}_{40}\text{Mn}_{40}\text{Cr}_{10}\text{Co}_{10}/10\%$  TiC composite (f)

**Table 3** Wear resistance properties of  $\text{Fe}_{40}\text{Mn}_{10}\text{Cr}_{10}\text{Co}_{10}$  MEA and  $\text{Fe}_{40}\text{Mn}_{10}\text{Cr}_{10}\text{Co}_{10}/10\%$  TiC composite

Alloy	Depth of wear track/ $\mu\text{m}$	Width of wear track/ $\mu\text{m}$	Friction coefficient
MEA	23.64	674.87	0.6
MEA/10% TiC	12.44	567.18	0.26

**Fig. 8** SEM images showing wear tracks on  $\text{Fe}_{40}\text{Mn}_{40}\text{Cr}_{10}\text{Co}_{10}$  MEA (a) and  $\text{Fe}_{40}\text{Mn}_{40}\text{Cr}_{10}\text{Co}_{10}/10\%$  TiC composite (d), high magnification SEM images of wear tracks on  $\text{Fe}_{40}\text{Mn}_{40}\text{Cr}_{10}\text{Co}_{10}$  MEA (b) and  $\text{Fe}_{40}\text{Mn}_{40}\text{Cr}_{10}\text{Co}_{10}/10\%$  TiC composite (e), and corresponding EDS pattern of denoted wear particle in (b) (c)**Fig. 9** XPS analysis results of  $\text{Fe}_{40}\text{Mn}_{40}\text{Cr}_{10}\text{Co}_{10}$  MEA in air: (a) Fe; (b) Mn; (c) Cr; (d) Co; (e) O

## 4 Discussion

### 4.1 Improvement in mechanical properties by adding TiC particles

The present study has confirmed that  $\text{Fe}_{40}\text{Mn}_{40}\text{Cr}_{10}\text{Co}_{10}/10\%$  TiC composite fabricated by powder

metallurgy with SPS exhibited improved mechanical properties in comparison with  $\text{Fe}_{40}\text{Mn}_{40}\text{Cr}_{10}\text{Co}_{10}$  MEA, as shown in Fig. 6.  $\text{Fe}_{40}\text{Mn}_{40}\text{Cr}_{10}\text{Co}_{10}/10\%$  TiC composite also presented superior comprehensive mechanical properties in counterpart with HEA/MEAs [17–19] and their based composites [12–13,20,21]. An orientation relationship (OR), i.e.,  $[011]//[\bar{1}22]$ ,

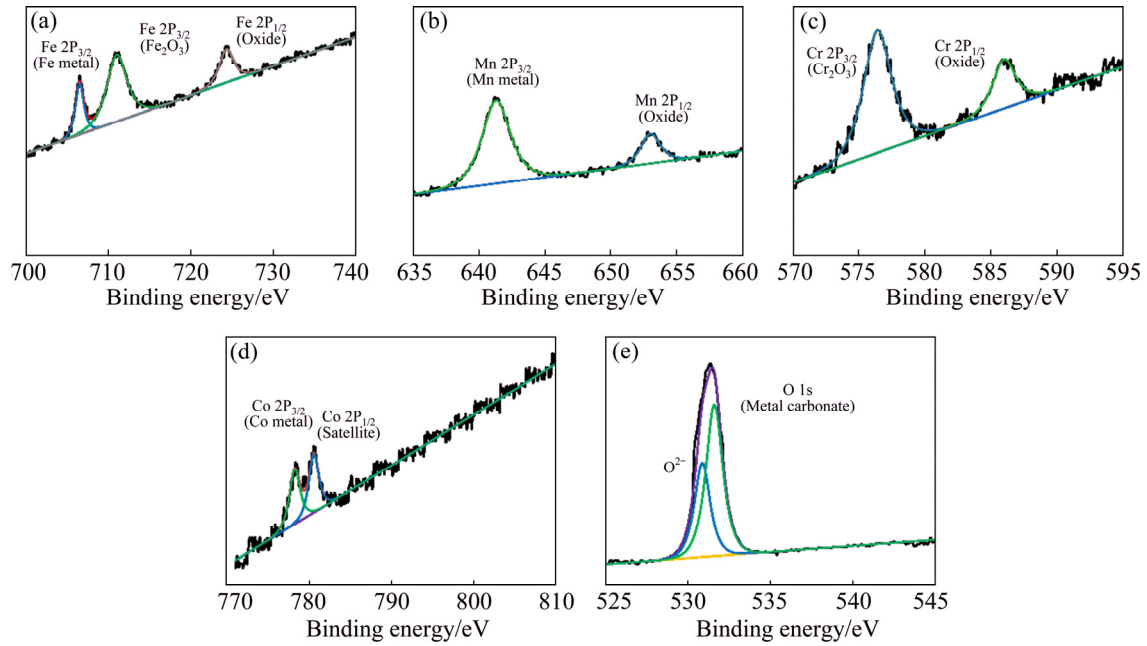


**Fig. 10** XPS analysis results of  $\text{Fe}_{40}\text{Mn}_{40}\text{Cr}_{10}\text{Co}_{10}/10\%$  TiC composite in air: (a) Fe; (b) Mn; (c) Cr; (d) Co; (e) O

$(\bar{1}\bar{1}\bar{1})//(\bar{0}2\bar{2})$ , was determined, as shown in Fig. 5(d). This OR indicates that a coherent interface  $(\bar{1}\bar{1}\bar{1})//(\bar{0}2\bar{2})$  exists between the matrix and the nanoscale particle. Thus, Orowan strengthening would be introduced through the TiC nanoscale particles. The addition of the TiC particles can inhibit the grain growth during sintering process and hinder dislocation motion during the deformation period. Grain refinement, effective load transfer effect and Orowan strengthening mechanism are responsible for these improved mechanical properties. In the following sections, the possible strengthening mechanisms will be discussed separately.

(1) The load transfer of interface between  $\text{Fe}_{40}\text{Mn}_{40}\text{Cr}_{10}\text{Co}_{10}$  and TiC particle

The load can transfer from matrix to the uniformly distributed reinforcement particles efficiently during deformation [22,23]. As depicted in Fig. 6(d), there are many voids left on the surface of the composite after TiC particles were pulled out. The interface can transfer load from  $\text{Fe}_{40}\text{Mn}_{40}\text{Cr}_{10}\text{Co}_{10}$  matrix to TiC effectively, which contributes to the improvement of the strength of  $\text{Fe}_{40}\text{Mn}_{40}\text{Cr}_{10}\text{Co}_{10}/10\%$  TiC composite. According to the modified shear lag model reported in Ref. [21], the strength contribution of load transfer effect in PRMMCs can be expressed by the following expression:

$$\Delta\sigma_{\text{Load}} = 0.5V_P \sigma_m \quad (1)$$

where  $\sigma_m$  is the yield strength of  $\text{Fe}_{40}\text{Mn}_{40}\text{Cr}_{10}\text{Co}_{10}$  MEA, as presented in Table 2.  $V_P$  is the volume fraction of the TiC particles. Equation (1) exhibits that  $\Delta\sigma_{\text{Load}}$  mainly

depends on the volume fraction of TiC particles. The increase in  $V_P$  brings a higher strength contribution.

(2) Orowan strengthening of TiC particles

$\sigma_{\text{Orowan}}$  can be calculated as follows [24]:

$$\sigma_{\text{Orowan}} = \frac{0.13Gb}{\lambda} \ln \frac{r}{2b} \quad (2)$$

where  $G$  is the shear modulus of matrix,  $b$  is the Burgers vector value,  $\lambda$  is the inter-particle spacing, and  $r$  is the radius of the particle. In present work, TiC particles are hard (the hardness is as high as HV 2000–3000), which incorporate with the soft ductile  $\text{Fe}_{40}\text{Mn}_{40}\text{Cr}_{10}\text{Co}_{10}$  MEA matrix and result in an increase in the hardness of the composite from HV 320 to HV 872 (see Table 2). These hard and dispersive particles are distributed to the grain boundaries and create resistance to dislocation propagation and movement. This suggests that higher shear stresses are needed to bypass dislocations through impeding the TiC particles, which eventually result in strengthening of the  $\text{Fe}_{40}\text{Mn}_{40}\text{Cr}_{10}\text{Co}_{10}/10\%$  TiC composite.

(3) Dislocation strengthening caused by the difference in coefficient of thermal expansion (CTE)

Large thermal mismatch stress can be generated owing to the difference in coefficient of thermal expansion between the matrix and the reinforcement during deformation [25,26]. Hence, a lot of thermal mismatch dislocations are generated in the composite to relax these thermal stresses. In present work, the CTEs of TiC particle and  $\text{Fe}_{40}\text{Mn}_{40}\text{Cr}_{10}\text{Co}_{10}$  MEA are  $7.4 \times 10^{-6}$  [27] and  $23 \times 10^{-6} \text{ K}^{-1}$  [28], respectively, which

lead to high dislocation density in  $\text{Fe}_{40}\text{Mn}_{40}\text{Cr}_{10}\text{Co}_{10}/\text{TiC}$  composite. These increased dislocations interact with each other, then impede their own motions and further increase the resistance to bypass the TiC particles.

(4) The grain refinement effect of TiC particle

The particles segregated at grain boundaries can provide a strong resistance between two neighboring grains. Grain boundary motion can be inhibited during sintering and achieve improved mechanical properties. For example, the grain size of CoCrFeNiMn MEA is decreased from 0.8 to 0.4  $\mu\text{m}$  by in-situ yttrium nano-oxides particles [29]. The addition of TiC particles, locating at the grain boundaries, can decrease the average grain size of the FCC phase, as indicated by the results of SEM and EBSD and theoretically described by the Zener pinning [30]. The grain size and the second phase particle size satisfy the following relationship:

$$d_m = 4\alpha d_p / 3v_{SP} \quad (3)$$

where  $d_m$  is the grain diameter,  $d_p$  is the second particle diameter,  $v_{SP}$  is the volume fraction of the second particle, and  $\alpha$  is the proportionality constant. This equation ties the grain radius of the matrix, the second particle diameter and volume fraction of the second particle so tightly together. Obviously, the decrease in  $d_p$  and the increase in  $v_{SP}$  bring a finer grain. This phenomenon has also previously been verified in Refs. [31–33].

#### 4.2 Improvement in friction performance by adding TiC particles

TiC-based ceramic metals have been reported to show a high abrasive wear resistance [34]. Figure 7 shows that the wear depth and friction coefficient of alloy decreased by adding TiC particles. The improvement in wear resistance of  $\text{Fe}_{40}\text{Mn}_{40}\text{Cr}_{10}\text{Co}_{10}/10\%$  TiC is attributed to the improved strength and hardness (see Table 2). TiC particles bonded with the FCC matrix and acted as plowing stopper to confine the soft FCC phases pulling out from the composite. Therefore, the hard TiC particles could protect the soft FCC matrix against the  $\text{Si}_3\text{N}_4$  balls during the sliding and the composite exhibited improved resistance and lower friction coefficient. ZHANG et al [35] found that the wear resistance of Fe–28Al–5Cr alloy was significantly improved by the addition of TiC and confirmed that the high hardness of TiC was the main reason. The wear resistance of Al2219 alloy was also reinforced by TiC particles at different loads and sliding distances [36]. The uniform distribution of TiC particulates in matrix enhanced the wear resistance of the composite.

## 5 Conclusions

(1)  $\text{Fe}_{40}\text{Mn}_{40}\text{Cr}_{10}\text{Co}_{10}/10\%$  TiC composites can be produced by powder metallurgy route through SPS at 1373 K for 15 min under 40 MPa.  $\text{Fe}_{40}\text{Mn}_{40}\text{Cr}_{10}\text{Co}_{10}$  MEA exhibits a single FCC phase and  $\text{Fe}_{40}\text{Mn}_{40}\text{Cr}_{10}\text{Co}_{10}/10\%$  TiC composite consists of FCC phase and TiC phase.

(2) Grain refinement is obtained by the addition of TiC in  $\text{Fe}_{40}\text{Mn}_{40}\text{Cr}_{10}\text{Co}_{10}$  MEA. The average grain size was 2.64  $\mu\text{m}$  for  $\text{Fe}_{40}\text{Mn}_{40}\text{Cr}_{10}\text{Co}_{10}/10\%$  TiC composite, which is finer than that for  $\text{Fe}_{40}\text{Mn}_{40}\text{Cr}_{10}\text{Co}_{10}$  MEA with an average grain size of 4.85  $\mu\text{m}$ .

(3) The significant increase in strength is achieved for  $\text{Fe}_{40}\text{Mn}_{40}\text{Cr}_{10}\text{Co}_{10}/10\%$  TiC composite. The compressive strength increases from 1.571 to 2.174 GPa and the hardness improves from HV 320 to HV 872 for  $\text{Fe}_{40}\text{Mn}_{40}\text{Cr}_{10}\text{Co}_{10}$  MEA and  $\text{Fe}_{40}\text{Mn}_{40}\text{Cr}_{10}\text{Co}_{10}/10\%$  TiC composite.

(4) Wear resistance of  $\text{Fe}_{40}\text{Mn}_{40}\text{Cr}_{10}\text{Co}_{10}/10\%$  TiC composite is superior to that of  $\text{Fe}_{40}\text{Mn}_{40}\text{Cr}_{10}\text{Co}_{10}$  MEA under the same condition. The wear modes in  $\text{Fe}_{40}\text{Mn}_{40}\text{Cr}_{10}\text{Co}_{10}$  MEA and  $\text{Fe}_{40}\text{Mn}_{40}\text{Cr}_{10}\text{Co}_{10}/10\%$  TiC composite include the micro-abrasive wear and oxidation wear.

## References

- [1] CHUN N G, GUO S, LUAN J H, SHI S Q, LIU C T. Entropy-driven phase stability and slow diffusion kinetics in an  $\text{Al}_{0.5}\text{CoCrCuFeNi}$  high entropy alloy [J]. *Intermetallics*, 2012, 31: 165–172.
- [2] CANTOR B, CHANG I, KNIGHT P, VINCENT A J B. Microstructural development in equiatomic multicomponent alloys [J]. *Materials Science and Engineering A*, 2004, 375–377: 213–278.
- [3] XIAO Wei-han, LU Shi-qiang, WANG Ya-chao, SHI Jing. Mechanical and tribological behaviors of graphene/Inconel 718 composites [J]. *Transactions of Nonferrous Metals Society of China*, 2018, 28: 1958–1969.
- [4] BUSHLYA V, LENRICK F, GUTNICHENKO O, PETRUSHA I, OSIPOV O. Performance and wear mechanisms of novel superhard diamond and boron nitride based tools in machining Al– $\text{SiC}_p$  metal matrix composite [J]. *Wear*, 2017, 376–377: 152–164.
- [5] ALIDOKHT S A, ABDOLLASH-ZADEH A, ASSADI H. Effect of applied load on the dry sliding wear behaviour and the subsurface deformation on hybrid metal matrix composite [J]. *Wear*, 2013, 305: 291–298.
- [6] SIVAKUMAR G, ANANTHI V, RAMANATHAN S. Production and mechanical properties of nano  $\text{SiC}$  particle reinforced Ti–6Al–4V matrix composite [J]. *Transactions of Nonferrous Metals Society of China*, 2017, 27: 82–90.
- [7] DAN C Y, CHEN Z, MATHON M H, JI G, LI L W. Cold rolling texture evolution of  $\text{TiB}_2$  particle reinforced Al-based composites by neutron diffraction and EBSD analysis [J]. *Materials Characterization*, 2018, 136: 293–301.

- [8] HUANG S J, PENG W Y, VISIC B, ZAK A. Al alloy metal matrix composites reinforced by WS<sub>2</sub> inorganic nanomaterials [J]. *Materials Science and Engineering A*, 2018, 709: 290–300.
- [9] JAVDANI A, DAEISORKHABI A H. Microstructural and mechanical behavior of blended powder semisolid formed Al7075/B<sub>4</sub>C composites under different experimental conditions [J]. *Transactions of Nonferrous Metals Society of China*, 2018, 28: 1298–1310.
- [10] YEH Chun-liang, CHEN Yi-chang. In situ formation of Zr<sub>2</sub>Al<sub>3</sub>C<sub>4</sub>/Al<sub>2</sub>O<sub>3</sub> composites by combustion synthesis with PTFE and thermal activations [J]. *Transactions of Nonferrous Metals Society of China*, 2018, 28: 2011–2016.
- [11] LIU W H, LU Z P, HE J Y, LUAN J H, WANG Z J, LIU B, LIU Y, CHEN M W, LIU C T. Ductile CoCrFeNiMo<sub>x</sub> high entropy alloys strengthened by hard intermetallic phases [J]. *Acta Materialia*, 2016, 116: 332–342.
- [12] ROGAL L, KALITA D, TARASEK A, BOBROWSKI A P, CZERWINSKI F. Effect of SiC nano-particles on microstructure and mechanical properties of the CoCrFeMnNi high entropy alloy [J]. *Journal of Alloy and Compounds*, 2017, 708: 344–352.
- [13] ROGAL L, KALITA D, LITYNSKA-DOBZYNSKA L. CoCrFeMnNi high entropy alloy matrix nanocomposite with addition of Al<sub>2</sub>O<sub>3</sub> [J]. *Intermetallics*, 2017, 86: 104–109.
- [14] COLOMBINI E, GUALTIERI M L, ROSA R, TARTERINI F, ZADRA M. SPS-assisted synthesis of SiC<sub>p</sub> reinforced high entropy alloys: Reactivity of SiC and effects of pre-mechanical alloying and post-annealing treatment [J]. *Powder Metallurgy*, 2017, 6: 1–9.
- [15] ZHANG A J, HAN J S, SU B, LI P D, MENG J H. Microstructure, mechanical properties and tribological performance of CoCrFeNi high entropy alloy matrix self-lubricating composite [J]. *Materials & Design*, 2016, 725: 700–710.
- [16] LI Z M, PRADEEP K G, DENG Y, RAABE D, TASAN C C. Metastable high-entropy dual-phase alloys overcome the strength–ductility trade-off [J]. *Nature*, 2016, 534: 227–230.
- [17] FAN J T, ZHANG L J, YU P F, ZHANG M D, LIU D J. Improved the microstructure and mechanical properties of AlFeCoNi high-entropy alloy by carbon addition [J]. *Materials Science and Engineering A*, 2018, 728: 30–39.
- [18] POHAN R M, GWALANI B, LEE J, ALAM T, HWANG J Y. Microstructures and mechanical properties of mechanically alloyed and spark plasma sintered Al<sub>0.3</sub>CoCrFeMnNi high entropy alloy [J]. *Materials Chemistry and Physics*, 2018, 210: 62–70.
- [19] SONG R K, YE F, YANG C X, WU S J. Effect of alloying elements on microstructure, mechanical and damping properties of Cr–Mn–Fe–V–Cu high-entropy alloys [J]. *Journal of Materials Science & Technology*, 2018, 34: 2014–2021.
- [20] CHEN H, CHEN W, LIU X Q, TANG Q H, XIE Y C. Effect of Ti and C additions on the microstructure and mechanical properties of the FeCoCrNiMn high-entropy alloy [J]. *Materials Science and Engineering A*, 2018, 719: 192–198.
- [21] FAN Q C, LI B S, ZHANG Y. The microstructure and properties of (FeCrNiCo)Al<sub>x</sub>Cu<sub>y</sub> high-entropy alloys and their TiC-reinforced composites [J]. *Materials Science and Engineering A*, 2014, 598: 244–250.
- [22] DONG H N, CHA S I, LIM B K, PARK H M, HAN D S. Synergistic strengthening by load transfer mechanism and grain refinement of CNT/Al–Cu composites [J]. *Carbon*, 2012, 50: 2417–2423.
- [23] RAMAKRISHNAN N. An analytical study on strengthening of particulate reinforced metal matrix composites [J]. *Acta Materialia*, 1996, 44: 69–77.
- [24] HOFMEISTER C, KLIMOV M, DELEGHANTY T, CHO K, SOHN Y. Quantification of nitrogen impurity and estimated Orowan strengthening through secondary ion mass spectroscopy in aluminum cryomilled for extended durations [J]. *Materials Science and Engineering A*, 2015, 648: 412–417.
- [25] TOROPOVA M M, STEEVES C A. Adaptive bimaterial lattices to mitigate thermal expansion mismatch stresses in satellite structures [J]. *Acta Astronautica*, 2015, 113: 132–141.
- [26] FEI W D, HU M, YAO C K. Thermal expansion and thermal mismatch stress relaxation behaviors of SiC whisker reinforced aluminum composite [J]. *Materials Chemistry and Physics*, 2013, 77: 882–888.
- [27] MEENASHISUNDARAM G K, GUPTA M. Synthesis and characterization of high performance low volume fraction TiC reinforced Mg nanocomposites targeting biocompatible/structural applications [J]. *Materials Science and Engineering A*, 2015, 627: 306–315.
- [28] LAPLANCHE G, GADAUD P, HORST O, OTTO F, EGGELER G. Temperature dependencies of the elastic moduli and thermal expansion coefficient of an equiatomic, single-phase CoCrFeMnNi high-entropy alloy [J]. *Journal of Alloy and Compounds*, 2015, 623: 348–353.
- [29] HADRABA H, CHLUP Z, DLOUHY A, DOBES F, ROUPCOVA P. Oxide dispersion strengthened CoCrFeNiMn high-entropy alloy [J]. *Materials Science and Engineering A*, 2017, 689: 252–256.
- [30] MOELANS N, BLANPAIN B, WOLLANTS P. Pinning effect of second-phase particles on grain growth in polycrystalline films studied by 3-D phase field simulations [J]. *Acta Materialia*, 2007, 55: 2173–2182.
- [31] DU J, YAO Z J, HAN S, LI W F. Discussion on grain refining mechanism of AM30 alloy inoculated by MgCO<sub>3</sub> [J]. *Journal of Magnesium and Alloy*, 2017, 5: 181–188.
- [32] LI X W, CAI Q Z, ZHAO B Y, LIU B, LIU B. Grain refining mechanism in pure aluminum with nanosized TiN/Ti composite refiner addition [J]. *Journal of Alloy and Compounds*, 2016, 699: 283–290.
- [33] FAN Z, WANG Y, ZHANG Y, QIN T, ZHOU X R. Grain refining mechanism in the Al/Al–Ti–B system [J]. *Acta Materialia*, 2015, 84: 292–304.
- [34] KOMAC M, NOVAK S. Mechanical and wear behavior of TiC cemented carbides [J]. *International Journal of Refractory Metals and Hard Materials*, 1985, 4: 21–26.
- [35] ZHANG X H, MA J Q, FU L C, ZHU S Y, LI F. High temperature wear resistance of Fe–28Al–5Cr alloy and its composites reinforced by TiC [J]. *Tribology International*, 2013, 61: 48–55.
- [36] HARTI J I, PRASAD T B, NAGARAL M, JADHAV P, AURADI V. Microstructure and dry sliding wear behaviour of Al2219–TiC composites [J]. *Materials Today: Proceedings*, 2017, 4: 11004–11009.

## Fe<sub>40</sub>Mn<sub>40</sub>Cr<sub>10</sub>Co<sub>10</sub>/TiC 中熵合金复合材料的力学和摩擦磨损性能

汪建英<sup>1</sup>, 方京华<sup>1</sup>, 杨海林<sup>1</sup>, 刘峙麟<sup>2</sup>, 李瑞迪<sup>1</sup>, Shou-xun Ji<sup>3</sup>, Yun WANG<sup>3</sup>, 阮建明<sup>1</sup>

1. 中南大学 粉末冶金国家重点实验室, 长沙 410083;

2. 中南大学 机电工程学院, 长沙 410083;

3. Institute of Materials and Manufacturing, Brunel University London,  
Uxbridge, Middlesex UB8 3PH, U. K.

**摘要:** 采用机械球磨和放电等离子烧结方法制备 Fe<sub>40</sub>Mn<sub>40</sub>Cr<sub>10</sub>Co<sub>10</sub>/TiC (TiC 的体积分数为 10%) 中熵合金复合材料, 并对其力学和摩擦磨损性能进行研究。研究表明, 在 1373 K 烧结 15 min 后, TiC 颗粒均匀分布在 Fe<sub>40</sub>Mn<sub>40</sub>Cr<sub>10</sub>Co<sub>10</sub>/TiC 复合材料中, 烧结后复合材料的晶粒得到明显细化; 同时, 添加 10% TiC 颗粒使复合材料的抗压强度从 1.571 GPa 提高至 2.174 GPa, 维氏硬度从 HV 320 提高至 HV 872。摩擦磨损试验表明, 与 Fe<sub>40</sub>Mn<sub>40</sub>Cr<sub>10</sub>Co<sub>10</sub> 中熵合金基体相比, 复合材料的摩擦因数、磨痕深度和宽度都减小。良好的力学性能和摩擦磨损性能使 Fe<sub>40</sub>Mn<sub>40</sub>Cr<sub>10</sub>Co<sub>10</sub>/TiC 复合材料成为工程应用的理想材料。

**关键词:** TiC; Fe<sub>40</sub>Mn<sub>40</sub>Cr<sub>10</sub>Co<sub>10</sub>/TiC 复合材料; 力学性能; 摩擦磨损性能; 放电等离子烧结

(Edited by Wei-ping CHEN)